A Johann-type X-ray emission spectrometer at the Rossendorf beamline

Kristina O. Kvashnina[a,b]* and Andreas C. Scheinost[a,b]

[a]Rossendorf Beamline at ESRF – The European Synchrotron, CS40220, 38043 Grenoble Cedex 9, France, and [b]Helmholtz Zentrum Dresden-Rossendorf (HZDR), Institute of Resource Ecology, PO Box 510119, 01314 Dresden, Germany. *Correspondence e-mail: kristina.kvashnina@esrf.fr

This paper gives a detailed description, including equations, of the Johann-type X-ray emission spectrometer which has been recently installed and tested at the Rossendorf beamline (ROBL) of the European Synchrotron Radiation Facility. The spectrometer consists of a single spherically bent crystal analyzer and an avalanche photodiode detector positioned on the vertical Rowland cycle of 1 m diameter. The hard X-ray emission spectrometer ($\sim$3.5–25 keV) operates at atmospheric pressure and covers the Bragg angles of 65°–89°. The instrument has been tested at high and intermediate incident energies, *i.e.* at the Zr K-edge and at the Au L_3-edge, in the second experimental hutch of ROBL. The spectrometer is dedicated for studying actinides in materials and environmental samples by high-energy-resolution X-ray absorption and X-ray emission spectroscopies.

1. Introduction

The community of synchrotron radiation users at hard X-ray absorption beamlines frequently requests access to X-ray emission spectrometers. There are several reasons for this current demand, which is expected to further increase in the future. First, compared with conventional methods, high-energy-resolution fluorescence detection (HERFD) (de Groot & Kotani, 2008) using an X-ray emission spectrometer allows X-ray absorption spectra to be recorded with substantially better energy resolution (Hämäläinen *et al.*, 1991), since the spectral broadening of the absorption features is drastically reduced in the case of the HERFD method (de Groot *et al.*, 2002). At the same time, the background, generated by other elements in the investigated materials, is minimized by the use of the crystal analyzer in the X-ray emission setup. Thus, the lower detection limit of elements can be considerably decreased, even in complex materials down to the lower p.p.m. level, and/or the counting time can be reduced (Kvashnina *et al.*, 2009). Finally, in the case of elements with little energy distance between their absorption edges (*e.g.* for neighboring lanthanides), the interference of these absorption edges can be eliminated in certain cases by a specific crystal analyzer (Hübner *et al.*, 2011).

Second, X-ray emission spectroscopy provides the possibility to record the valence and core X-ray emission lines with resonant and non-resonant excitations (Glatzel & Bergmann, 2005; Vankó *et al.*, 2006; Kvashnina *et al.*, 2014). This becomes very important when investigating the ligand orbitals of a selected element and the crystal structure of materials (Safonov *et al.*, 2006; Smolentsev *et al.*, 2009). There are also other techniques which could be developed, when X-ray

emission spectrometers are more freely available, such as non-resonant (Raman) X-ray scattering (Krisch & Sette, 2002). This method allows the soft X-ray transitions to be probed by the incident hard X-rays. Unfortunately, the cross section of this process is very low and requires technical improvements for emitted energy paths (*e.g.* a multiple crystal analyzer setup).

Technically, an X-ray emission spectrometer consists of a crystal analyzer and a detector, which can be realized with different geometries. The most renowned types are the Johannson (Johansson, 1933), Johann (Johann, 1931) and von Hamos (von Hamos, 1932) geometries. The existence of various geometries provides the opportunity to build the most appropriate instrument for the particular experimental station. In the case of Johann and Johannson geometries, a point-to-point focusing scheme is realized, where both the crystal analyzer and the detector are moved when the emitted energy is scanned (Bergmann & Cramer, 1998; Huotari *et al.*, 2006; Hazemann *et al.*, 2009; Kleymenov *et al.*, 2011; Kavčič *et al.*, 2012; Sokaras *et al.*, 2013). This scheme provides a higher detection signal, and covers a larger solid angle. In contrast, the possibility of recording the emission lines with the energy-dispersive (von Hamos) geometry is very practical since it does not include movable parts (Szlachetko *et al.*, 2012). Here, we show the implementation of a very simple Johann-type X-ray emission spectrometer with a single spherically bent crystal analyzer and provide the equations for the calculation of the positions of the crystal analyzer and the detector in the X-ray emission setup. This setup was tested at the Rossendorf beamline for actinide research. Installation of a multiple crystal analyzer instrument with different Rowland cycle diameters is foreseen in 2017.

2. Technical details

A single-crystal X-ray emission spectrometer with vertical scattering geometry was mounted in the second experimental hutch of the Rossendorf beamline (Matz *et al.*, 1999) and tested at intermediate ($\sim$11 keV) and high ($\sim$18 keV) energies. The incident energy was selected using the (111) reflection from a double Si crystal monochromator. For the Zr *K*-edge measurements, the beam was both vertically and horizontally focused with the Rh-coated toroidal section of the mirror after the monochromator, while for the Au L_3-edge measurements we used the sagittally flat Si surface of this mirror, *i.e.* obtaining only vertical focusing. In both cases, the mirror was set at an incident angle of 2.5 mrad. The incident monochromatic X-ray beam has a flux of $\sim$10^{11} photons s^{-1} on the sample position at an energy of 12 keV, with a beam size of 150 μm × 400 μm (V × H). All samples were measured simultaneously in HERFD mode by reflecting the detected beam with the single-crystal analyzer, and directly in total fluorescence yield (TFY) mode using a Canberra photodiode. Incident energy was scanned by the monochromotor and two signals for XANES measurements were collected at the same time in HERFD and TFY modes.

The X-ray emission spectrometer consists of the crystal analyzer and the detector, which are located together with the sample on the Rowland cycle. The HERFD measurement is then performed by scanning the incident energy across the absorption edge of the selected element at the maximum of the X-ray emission line. X-ray emission spectra are measured by scanning the emitted energy with the crystal analyzer, while keeping the incident energy fixed. If the incident energy is selected above the X-ray absorption edge, non-resonant X-ray emission spectra are recorded. If the incident energy is selected below or near the absorption edge, resonant X-ray emission spectra or resonant inelastic X-ray scattering is recorded.

The basic principle of the spectrometers is that the energy of the emitted fluorescence is selected by the Bragg reflection of the crystal analyzer. According to Bragg's law,

$$2d \sin \Theta = n\lambda, \tag{1}$$

where Θ is the scattering angle, d is the lattice spacing for the given crystal orientation, n is the order of reflection, and λ is the wavelength of the X-ray photons. For a crystal with cubic symmetry, the d-spacing for a given crystal orientation can be obtained through the following equation:

$$d = \frac{a}{(h^2 + k^2 + l^2)^{1/2}}, \tag{2}$$

where a is the lattice spacing and h, k, l are the Miller indices of the Bragg plane.

The tabulated lattice parameters for common crystals are:

$$a = 5.6574 \, \text{Å} \quad \text{for germanium (Ge)},$$
$$a = 5.4309 \, \text{Å} \quad \text{for silicon (Si)}. \tag{3}$$

In this case, the Bragg angle for any energy (E in keV) is calculated using the following equation:

$$\Theta = \arcsin \frac{6.19926 \, n}{dE}. \tag{4}$$

A schematic drawing of a typical Rowland circle setup is shown in Fig. 1. The centers of sample, bent crystal analyzer and detector are all located on a Rowland cycle with radius R. The bent crystal analyzer with a fixed radius of $2R$ reflects the fluorescence X-rays from the sample to the detector. The detector has to be shifted along the Rowland cycle, once the Bragg angle Θ or the emitted energy is changed. At the same time, the angle of the bent crystal analyzer has to be changed.

To enable these movements of the crystal analyzer and the detector along a vertical Rowland circle, we have established a mechanical setup as shown in Fig. 2. During a measurement, the sample rests always at the same place. The distance SC between the sample and the center of the crystal analyzer is kept equal to the distance CD between the center of the crystal analyzer and the center of the detector,

$$\text{SC} = \text{CD} = 2R \sin \Theta. \tag{5}$$

In order to keep the focusing geometry, the detector has to be maintained at an angle (Ω), which is twice the angle of the crystal analyzer (Θ),
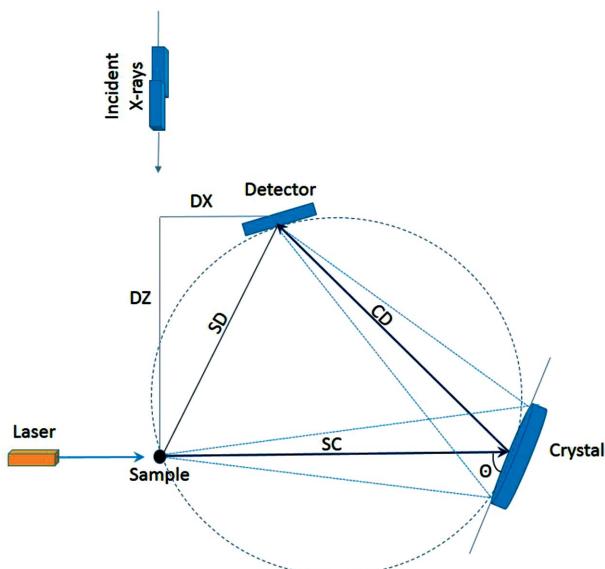
Figure 1
Schematic drawing of the Johann-type X-ray emission spectrometer.

$$\Omega = 2\Theta. \qquad (6)$$

The detector, an avalanche photodiode (APD) of 200 µm thickness, has been mounted on a goniometer, which in turn is mounted on two linear stages marked DX and DZ in Fig. 2 arranged perpendicularly. The distances DX and DZ are calculated according to the following formulas:

$$DZ = 2 \times SC \times \sin\frac{(90-\Theta)\pi}{180} \times \cos\frac{(90-\Theta)\pi}{180} \qquad (7)$$

and

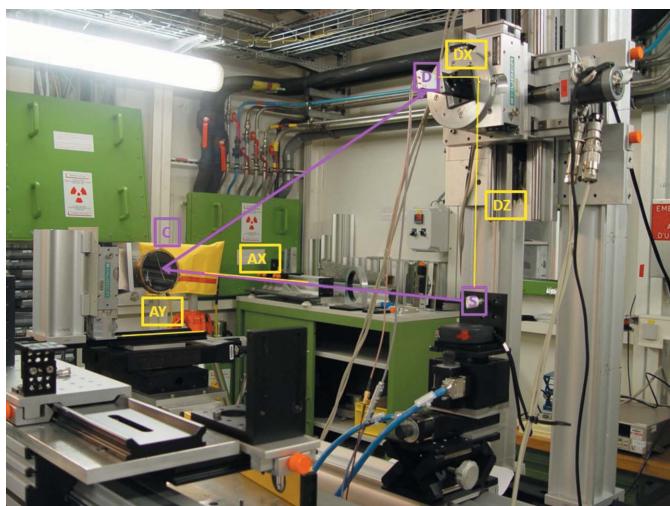$$DX = 2 \times SC \times \sin^2\frac{(90-\Theta)\pi}{180}. \qquad (8)$$

Figure 2
Photograph of the X-ray emission spectrometer setup at the Rossendorf beamline. The positions of the sample (S), crystal (C) and the detector (D) are marked by the respective letters in pink. The linear stages of the crystal analyzer and the detector are shown in yellow and marked as AX, AY and DX, DY

Table 1
Calculated positions of the motors in the X-ray emission setup for the maximum of the Zr $K\alpha_1$ and the Au $L\alpha_1$ emission lines.

	Emission line	
	Zr $L\alpha_1$	Au $L\alpha_1$
Tabulated value	15.775 keV	9.713 keV
Crystal analyzer	Ge 220	Ge 111
Reflection (n)	5	5
Bragg angle Θ	79.22°	77.69°
AX	982.355 mm	977.013 mm
Detector angle Ω	158.44°	155.38°
DZ	360.963 mm	406.983 mm
DX	68.721 mm	88.802 mm

Like the detector, the crystal analyzer is also mounted on a goniometer and two linear stages in perpendicular geometry. The goniometer is used to position the crystal at the angle Θ. The AX linear stage moves the crystal analyzer in the SC direction (Fig. 1), and the AY stage is mounted perpendicular to AX. The second linear stage (AY) can be replaced by the goniometer and has to be used to guide the reflected X-rays from the crystal analyzer to the middle of the detector in the horizontal plane.

During the first experiment, the Zr K- and Au L_3-edges have been measured at the maximum of the most intense $K\alpha_1$ and $L\alpha_1$ emission lines, respectively. Two types of spherically bent crystal analyzers have been used: Ge (220) for the Zr $K\alpha_1$ line, and Ge (111) for the Au $L\alpha_1$ line, each with a bending radius of 1 m. The calculated positions of all motors for both emission lines are summarized in Table 1.

For the pre-alignment of all components, and to test their proper coordinated movement along the Rowland circle, and their orientation towards the detector, we used the following laser setup. The laser itself was mounted perpendicular to the direction of the X-ray beam and behind the sample stage (Fig. 1). A non-transparent tape was mounted on the sample stage in order to scatter the laser beam. First, the scattering angle (Θ) of 90° was precisely determined using the laser reflection by placing the crystal analyzer at 90° and adjusting the angle of the goniometer. The scattering from the tape should match the position of the laser reflection at $\Theta = 90°$. Second, the position of the crystal analyzer at the correct radius of the Rowland circle was adjusted using the laser. When the crystal is placed at $\Theta = 90.2°$, the reflected light from the crystal is seen a few millimeters below the sample position (or the laser reflection of the tape). The motion of the crystal in the SC direction (AX motor) adjusts then the radius of the crystal analyzer. Third, the detector was placed in the focus of the crystal analyzer by using the laser light scattering as well. The crystal analyzer was moved to the estimated Bragg angle ($\sim$79.22° for the Zr $K\alpha_1$, and 77.69° for Au $L\alpha_1$ measurements). By moving the DX and DZ motors, the detector was then centered in the laser beam.

After this laser pre-alignement, the alignment was refined with the X-ray beam by using the emitted fluorescence of the test samples. We performed three scans: a Θ scan in the range $\pm0.2°$, an AY scan in the range ±5 mm, and then another Θ scan with a finer step size using the Zr (and Au) foils. The
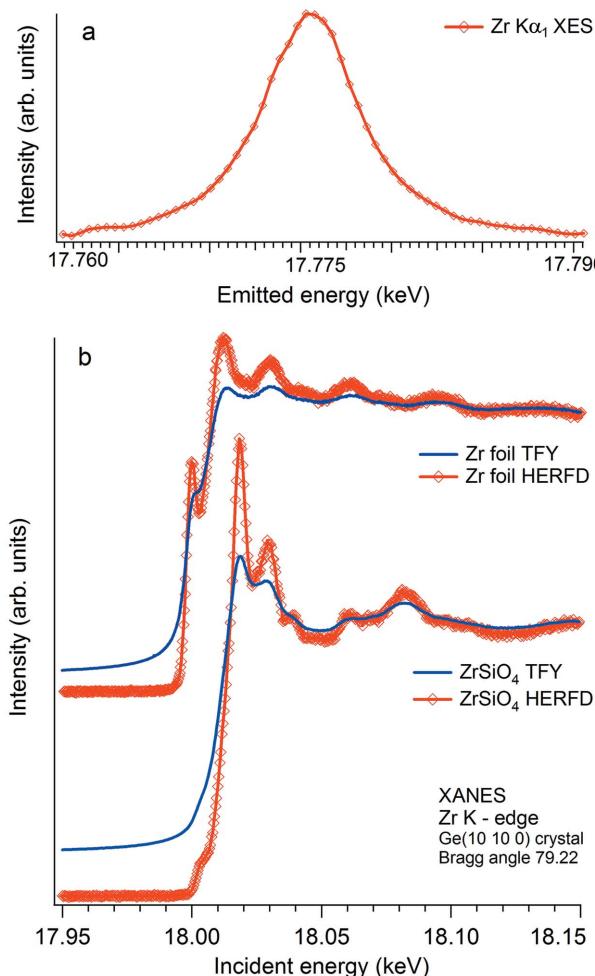
Figure 3
(*a*) Zr $K\alpha_1$ X-ray emission spectrum recorded on the Zr foil. (*b*) Zr *K*-edge XANES spectra of the Zr foil and of $ZrSiO_4$ powder recorded in HERFD (red) and TFY (blue) modes simultaneously.

emission energy was scanned by moving simultaneously the AY, Θ, Ω, DX and DZ motors. Finally, the sample was scanned in the direction of the incident energy in order to place the sample in the focus of the crystal analyzer. A scan of the emission energy near the maximum of the Zr $K\alpha_1$ line at an incident energy of 18.2 keV is shown in Fig. 3(*a*). The broadening of the emission line, determined as half width at half-maximum, is $\sim$5.5 eV.

3. Examples

The Zr *K*-edge XANES spectra of a Zr foil and of $ZrSiO_4$ powder are shown in Fig. 3(*b*). Both samples were measured simultaneously in TFY and in HERFD modes at the maximum of the Zr $K\alpha_1$ emission line. We did not find any difference in the value of the maximum of the Zr $K\alpha_1$ emission line between different samples. Therefore, the X-ray emission spectrometer was not moved during the HERFD data collection on both samples. The main features in the Zr *K*-edge XANES correspond to the dipole-allowed transitions from the 1*s* to the 5*p* states. The improved resolution of the HERFD spectra allows

identification of the clearly separated pre-edge structure in the spectra of both Zr compounds, which arises from the dipole-forbidden but quadrupole-allowed transitions between 1*s* and 4*d* states. The pre-edge features indicate the distortion of the crystal structure of the solids and show the effect of the hybridization between the *d*, *p* states of Zr and the unoccupied states of the ligands. The HERFD spectra collected at the Rossendorf beamline are in good agreement with the HERFD spectra previously recorded by Wilke and co-authors at the dedicated XES beamline of the European Synchrotron Radiation Facility (ESRF), ID26 (Wilke *et al.*, 2012). The only difference is that Wilke and co-authors used a pair of Si (311) crystals in the monochromator, which have a better incident energy resolution.

Fig. 4 shows the Au L_3-edge XANES spectrum of the Au foil recorded in TFY and HERFD mode simultaneously. The achieved energy resolution of the HERFD spectrum matches previously reported results also collected at ID26 (Erenburg *et al.*, 2013). The intensity of the recorded HERFD and X-ray emission spectrum was significantly lower compared with the measurements at higher incident energy (Zr *K*-edge) due to the considerable absorption of X-rays by air. We plan to reduce the air paths in the space between the sample, analyzer and the detector in the near future.

The energy resolution of the spectra can be further improved by placing a slit in front of the detector. The count rate can be further increased by installation of a crystal analyzer with a bending radius of 0.5 m (the signal is expected to be four times higher than in case of the crystal with a 1 m bending radius). These options will be realized together with a multiple-crystal X-ray emission setup at the Rossendorf beamline at the end of 2017.

The count rate for the emitted energies above 11 keV can be further improved by using a CdZnTe or other detector with higher sensitivity for higher X-ray energies. There is another possibility of increasing the signal-to-noise ratio, by moving the crystal analyzer inside the Rowland cycle (Kavčič *et al.*, 2012). The total energy resolution will decrease, but the sharpening effect of the HERFD data remains strong. Especially in cases where wide emission lines are used for HERFD
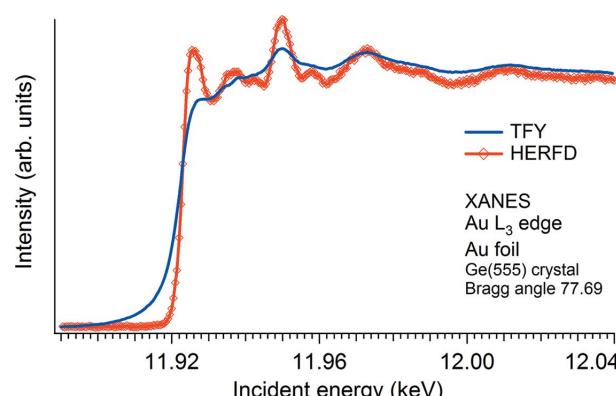

Figure 4
Au L_3-edge XANES spectra of the Au foil recorded in HERFD (red) and TFY (blue) modes simultaneously.

beamlines

data collection, the loss of the energy resolution has little influence on the energy resolution of the HERFD spectra, while improving the count rate drastically

4. Conclusions

This manuscript gives an overview of an X-ray emission setup which can be constructed at any X-ray absorption beamline in a relatively short time. It includes the single-crystal analyzer, the detector, four linear stages and two goniometers. The signal-to-noise ratio can be improved by installing several crystal analyzers in a row, as realized for instance at the ESRF beamlines ID26 (Glatzel *et al.*, 2013), ID20 (Huotari *et al.*, 2006) and FAME (Hazemann *et al.*, 2009), at the SLS beamline SuperXAS (Kleymenov *et al.*, 2011), the ANKA beamline INE and the SSRL beamline 6-2 (Sokaras *et al.*, 2013).

Such X-ray emission spectrometers can be used as complimentary instruments on any beamline. The possibility of using the X-ray emission setup not only in a monochromatic but also in a pink beam has been already demonstrated (Rueff *et al.*, 1999). The spectrometer is very compact and can be placed at any position near the sample. Vertical or horizontal Rowland geometries might be chosen depending on the beamline requirements and restrictions. The electronic structure information is very important and related to all types of experiments, such as diffraction, scattering, imaging, *etc*. The possibility of studying the investigated systems by different techniques simultaneously is therefore heavily requested by the user communities at many synchrotron radiation sources.

5. Future plans

We show here the first data measured at the Rossendorf beamline by a single-crystal Johann-type X-ray emission spectrometer. The spectrometer will be further developed for studying nuclear waste materials and environmental applications (Vitova *et al.*, 2010; Kvashnina *et al.*, 2013, 2014; Kvashnina & de Groot, 2014). The current bulk X-ray absorption fine-structure station of the ROBL is equipped as an alpha-lab and allows actinides and other radionuclides up to 185 MBq (Fig. 5) to be studied. Due to the spatial restrictions of the current alpha-glovebox, the X-ray emission spectrometer could only be installed in a second hutch, which does not provide inherent protection from alpha-emitting radionuclides. Therefore, only samples in line with the standard ESRF safety regulations for experiments with radioactive samples can be currently measured. The maximum activity per sample under these conditions can be found at the ESRF website. These are for instance 640 kBq for Np-237,

Tc-99	Po-208	Po-209	Ra-226	Th-nat	Pa-231
29 100	0.008	0.3	5	10^6	106
U-nat	Np-237	Pu-238	Pu-239	Pu-240	Pu-241
10^6	6 997	0.29	80	22	0.049
Pu-242	Am-241	Am-243	Cm-244	Cm-246	Cm-248
1 240	1.4	25	0.062	17	1 156

Figure 5
List of radionuclides and amount in mg to stay below the maximum activity limit of 185 MBq permitted on ROBL.

300 kBq for Pu-238, and 340 kBq for Am-241 in the solid state. The maximum total activity of all the samples is restricted to 3.7 MBq. To overcome this restriction, the second experimental ROBL hutch containing the X-ray emission spectrometer will also be converted into an alpha-lab in 2018–2019 (Fig. 6). Both experimental hutches will be connected by a lock room, which allows an easy transfer of radionuclide samples between them, and therefore an easy access to the full array of experimental techniques available at the beamline. The maximum activity given in Fig. 5 will then be valid for all samples and all techniques.

We plan to study nuclear materials as liquids and solids with the help of the X-ray emission spectrometer. A special cell will be designed in order to handle radioactive liquid materials. A special cell will be provided for the *in situ* studies of nuclear materials at low temperatures down to 10 K, with laser excitations (pump and probe experiments) and at room temperature. In certain cases, we will be able to perform high-pressure experiments on single-crystal materials containing actinides. Due to the safety regulations of ESRF, high-temperature experiments on nuclear materials are forbidden.

All electronic transitions in the energy range between 5 and 35 keV can be studied in the high-energy-resolution mode at the ROBL beamline. This includes the actinide and lanthanide
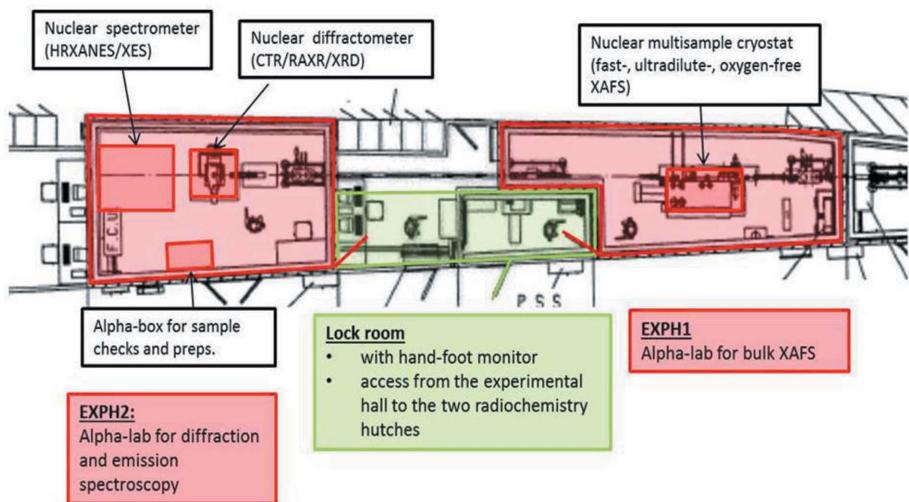

Figure 6
The two experimental hutches of ROBL (marked in red) will be equipped as alpha-labs and connected by a lock room (green). This will allow for an easy transfer of radionuclide samples between both stations to investigate them with the full array of experimental methods available, including the new spectrometer.

L-edges and transition metal *K*-edge absorption transitions. The main effort will be on studies of the core level transitions by means of the valence band XES and RIXS techniques, thanks to the high incident X-ray flux, which will be available for users after the ESRF EBS upgrade programme in 2018.

References

Bergmann, U. & Cramer, S. P. (1998). *Proc. SPIE*, **3448**, 198–209.

Erenburg, S. B., Trubina, S. V., Kovalenko, E. A., Geras'ko, O. A., Zaikovskii, V. I., Kvashnina, K. & Nikitenko, S. G. (2013). *JETP Lett.* **97**, 285–289.

Glatzel, P. & Bergmann, U. (2005). *Coord. Chem. Rev.* **249**, 65–95.

Glatzel, P., Weng, T.-C., Kvashnina, K., Swarbrick, J., Sikora, M., Gallo, E., Smolentsev, N. & Mori, R. A. (2013). *J. Electron Spectrosc. Relat. Phenom.* **188**, 17–25.

Groot, F. de & Kotani, A. (2008). *Core Level Spectroscopy of Solids.* Boca Raton: CRC Press.

Groot, F. M. F. de, Krisch, M. & Vogel, J. (2002). *Phys. Rev. B*, **66**, 195112.

Hämäläinen, K., Siddons, D. P., Hastings, J. B. & Berman, L. E. (1991). *Phys. Rev. Lett.* **67**, 2850–2853.

Hámos, L. von (1932). *Naturwissenschaften*, **20**, 705–706.

Hazemann, J.-L., Proux, O., Nassif, V., Palancher, H., Lahera, E., Da Silva, C., Braillard, A., Testemale, D., Diot, M.-A., Alliot, I., Del Net, W., Manceau, A., Gélébart, F., Morand, M., Dermigny, Q. & Shukla, A. (2009). *J. Synchrotron Rad.* **16**, 283–292.

Hübner, M., Koziej, D., Bauer, M., Barsan, N., Kvashnina, K., Rossell, M. D., Weimar, U. & Grunwaldt, J.-D. (2011). *Angew. Chem. Int. Ed.* **50**, 2841–2844.

Huotari, S., Albergamo, F., Vankó, G., Verbeni, R. & Monaco, G. (2006). *Rev. Sci. Instrum.* **77**, 053102.

Johann, H. H. (1931). *Z. Phys.* **69**, 185–206.

Johansson, T. (1933). *Z. Phys.* **82**, 507–528.

Kavčič, M., Budnar, M., Mühleisen, A., Gasser, F., Žitnik, M., Bučar, K. & Bohinc, R. (2012). *Rev. Sci. Instrum.* **83**, 033113.

Kleymenov, E., van Bokhoven, J. A., David, C., Glatzel, P., Janousch, M., Alonso-Mori, R., Studer, M., Willimann, M., Bergamaschi, A., Henrich, B. & Nachtegaal, M. (2011). *Rev. Sci. Instrum.* **82**, 065107.

Krisch, M. & Sette, F. (2002). *Surf. Rev. Lett.* **9**, 969–976.

Kvashnina, K. O., Butorin, S. M., Cui, D., Vegelius, J., Puranen, A., Gens, R. & Glatzel, P. (2009). *J. Phys. Conf. Ser.* **190**, 012191.

Kvashnina, K. O., Butorin, S. M., Martin, P. & Glatzel, P. (2013). *Phys. Rev. Lett.* **111**, 253002.

Kvashnina, K. O. & de Groot, F. M. F. (2014). *J. Electron Spectrosc. Relat. Phenom.* **194**, 88–93.

Kvashnina, K. O., Kvashnin, Y. O. & Butorin, S. M. (2014). *J. Electron Spectrosc. Relat. Phenom.* **194**, 27–36.

Matz, W., Schell, N., Bernhard, G., Prokert, F., Reich, T., Claußner, J., Oehme, W., Schlenk, R., Dienel, S., Funke, H., Eichhorn, F., Betzl, M., Pröhl, D., Strauch, U., Hüttig, G., Krug, H., Neumann, W., Brendler, V., Reichel, P., Denecke, M. A. & Nitsche, H. (1999). *J. Synchrotron Rad.* **6**, 1076–1085.

Rueff, J.-P., Kao, C.-C., Struzhkin, V. V., Badro, J., Shu, J., Hemley, R. J. & Mao, H. K. (1999). *Phys. Rev. Lett.* **82**, 3284–3287.

Safonov, V. A., Vykhodtseva, L. N., Polukarov, Y. M., Safonova, O. V., Smolentsev, G., Sikora, M., Eeckhout, S. G. & Glatzel, P. (2006). *J. Phys. Chem. B*, **110**, 23192–23196.

Smolentsev, G., Soldatov, A. V., Messinger, J., Merz, K., Weyhermüller, T., Bergmann, U., Pushkar, Y., Yano, J., Yachandra, V. K. & Glatzel, P. (2009). *J. Am. Chem. Soc.* **131**, 13161–13167.

Sokaras, D., Weng, T.-C., Nordlund, D., Alonso-Mori, R., Velikov, P., Wenger, D., Garachtchenko, A., George, M., Borzenets, V., Johnson, B., Rabedeau, T. & Bergmann, U. (2013). *Rev. Sci. Instrum.* **84**, 053102.

Szlachetko, J., Nachtegaal, M., de Boni, E., Willimann, M., Safonova, O., Sa, J., Smolentsev, G., Szlachetko, M., van Bokhoven, J. A., Dousse, J.-C., Hoszowska, J., Kayser, Y., Jagodzinski, P., Bergamaschi, A., Schmitt, B., David, C. & Lücke, A. (2012). *Rev. Sci. Instrum.* **83**, 103105.

Vankó, G., Neisius, T., Molnár, G., Renz, F., KÁRPáti, S., Shukla, A. & de Groot, F. M. F. (2006). *J. Phys. Chem. B*, **110**, 11647–11653.

Vitova, T., Kvashnina, K., Nocton, G., Sukharina, G., Denecke, M., Butorin, S., Mazzanti, M., Caciuffo, R., Soldatov, A., Behrends, T. & Geckeis, H. (2010). *Phys. Rev. B*, **82**, 235118.

Wilke, M., Schmidt, C., Dubrail, J., Appel, K., Borchert, M., Kvashnina, K. & Manning, C. E. (2012). *Earth Planet. Sci. Lett.* **349–350**, 15–25.